Optimization of measurement geometry for GASMAS lung function monitoring of infants

In collaboration with:

GPX Medical and

Division of Combustion Physics at LTH

LUND UNIVERSITY

Thesis by Dennis Leander

Spring semester 2017

1 Abstract

A technique for measuring oxygen concentration in the lungs of preterm infants is one of the latest advancements in neonatal care. It is called GAs in Scattering Media Absorption Spectroscopy (GASMAS) and enables non-invasive, bed-side monitoring of the lung function of our most fragile patients, preterm newborns. The technique is promising and its potential is now evaluated in preparation for clinical studies. This thesis work contains simulations performed on two newly developed 3D-printed models. One model is of the lungs with surrounding tissue and the other model is of the full chest region of a preterm infant. The lung model measurements concluded the GASMAS technique to measure oxygen concentration within 4 % for absorption pathlengths longer than 2 cm. The absorption pathlength was determined to be 20 % longer for the laser wavelength of 761 nm in comparison to 820 nm due to more scattering in the liquid tissue phantom. The measurements of the infant model concluded the most preferable laser and detector positions to be a geometry from the armpit to the chest where oxygen concentration could be determined within 2 percentage points for an absorption pathlength of 10 cm. An opportunity of measuring in-vivo on a three week old baby was also made possible where oxygen could be detected for the earlier mentioned geometry of armpit to chest. Even though the detected signal for the in-vivo tests was weak and the detected absorption pathlength too short for reliable oxygen concentration estimation to be made at this time, the results of this thesis further heightening the anticipation of GASMAS for lung monitoring to advance from laboratory proven to being verified in a clinical study.

Contents

2 Introduction

When an infant is born preterm, its organs are not fully mature. The lungs are among the more sensitive organs and do often need medical aid to transport enough oxygen into the blood stream to ensure a healthy growth of the baby. The first days after a preterm birth are crucial for the future well-being of the baby. It is also a time with high risk for the infant to be affected by Respiratory distress syndrome (RDS), a lung disease which comes from underdeveloped lungs and insufficient surfactant for the alveoli (protein to help keeping surface tension to maximize oxygen exchange between lungs and blood stream). The disease is closely related to early births where approximately 90 % of the children born in gestational weeks 22-28 are affected [15]. Even though X-rays are more harmful to new born babies than to adults, chest X-ray is still considered as a standard method for diagnosing premature RDS patients of today and is used for recurring checks on the lungs function. Neonatal care improves and babies born in gestational age as early as in week 20 have the possibility of a normal, healthy life. With these improvement, the need for a more effective monitoring of the lung functions is vital to handle more preterm babies with underdeveloped respiratory function and RDS to truly ensure the critical oxygenation of the blood.

Gas in Scattering Media Absorption Spectroscopy, GASMAS, is a promising technique for the future monitoring of gaseous cavities in the body. Smart measurements of the molecular absorption of the light from diode lasers in the lungs gives feedback of quantitative gaseous content with a bed-side, real time and noninvasive technique. A study by *E. Krite Svanberg et al.* [16] proved GASMAS to be able to detect pulmonary oxygen in all of the 29 new born full-term babies included in the study. This thesis aims to further test the technique and to develop means of system verification by simulated measurements rather than with in-vivo measurements. Following from the work done by Jim Larsson [4] and Peilang Liao [5] with an anatomical model of a preterm baby, this thesis will further develop the models for simulated lung measurements and optimize measurement geometries to be used for in-vivo measurements. As part of an EU financed effort to improve neonatal critical care, this work led by GPX Medical in Lund, is assisting the development of a pre-prototype GASMAS system for clinical studies.

2.1 Goals of the thesis

Preparation phase

- Support GPX Medical in constructing an initial prototype for lung function monitoring.
- Design and produce a simplified phantom to simulate lung-tissue geometry.
- Further develop an existing anatomically designed 3D-printed tissue phantom of a preterm infant and take it to production. Original design by Jim Larsson [4] and Peilang Liao [5].

- Develop recipe for preparation of a liquid tissue phantom resembling the optical properties of fat, muscle and heart muscle.

Measurement phase

- Calibrate and verify performance of pre-prototype for oxygen and water vapor concentration estimation.
- Measure oxygen concentration quantitatively in the simplified tissue phantom.
- Measure oxygen concentration quantitatively in an anatomically designed 3D-printed tissue phantom.
- Acquire measurable signal from in-vivo measurements of a newborn baby.

3 Optical properties of tissue

Human tissue, milk and clouds in the sky are examples of turbid media. They appear nontransparent to the eye but can still brightly be lit up because of their relatively low absorption and strong scattering of light. They contain randomly distributed particles of different refractive indices, n, which changes the incident propagation direction of the photons. The photons are scattered in the media. A small fraction of the photons are also sporadically absorbed by the media and are therefore not detectable.

3.1 Tissue optics

The propagation of light in turbid media can be described by optical properties such as the scattering coefficient, μ_s [cm^{-1}] and the absorption coefficient, μ_a [cm^{-1}], which denotes the inverse of the average distance between consecutive scattering and absorption events, respectively. The scattering direction is dependent on the direction of the incident light. In tissue there is, usually, a higher probability for the light from a single scattering event to be forward scattered, i.e. the scattering is non-isotropic. Therefore it is often more interesting to talk about the reduced scattering coefficient, μ_s' [cm^{-1}],

$$\mu_s' = (1 - g)\mu_s \tag{1}$$

where g is the scattering anisotropy, which is the average of the cosine of the photons' scattering angle. The amount of light reaching the detector is dependent on both the reduced scattering and the absorption. Therefore it is of interest to talk about the extinction coefficient, μ_e [cm^{-1}],

$$\mu_e = \mu_a + \mu_s' \tag{2}$$

where the ratio between scattering and extinction is the single scattering albedo, w_0, and is a measure of how the light extinction depends on the scattering.

$$\omega_0 = \frac{\mu_e - \mu_a}{\mu_e} \tag{3}$$

For tissue, as a highly scattering medium, the extinction coefficient is mostly determined by scattering, that is a single scattering albedo close to one. There are however components of the tissue with more significant absorption. The most important absorbers are found in figure 1. Oxyhemoglobin, HbO_2, and deoxyhemoglobin, Hb, are of high concentration in the blood, which gives rise to high absorption of light for wavelengths below 600 nm. Water, H_2O, another molecule of high concentration in the tissue, is the dominant absorber for wavelengths above 1300 nm. The wavelength interval between these two absorbers, around 600 to 1300 nm is advantageous for optical tissue measurements due to the relatively low light attenuation and is known as "the tissue optical window" (shadowed red area in figure 1).

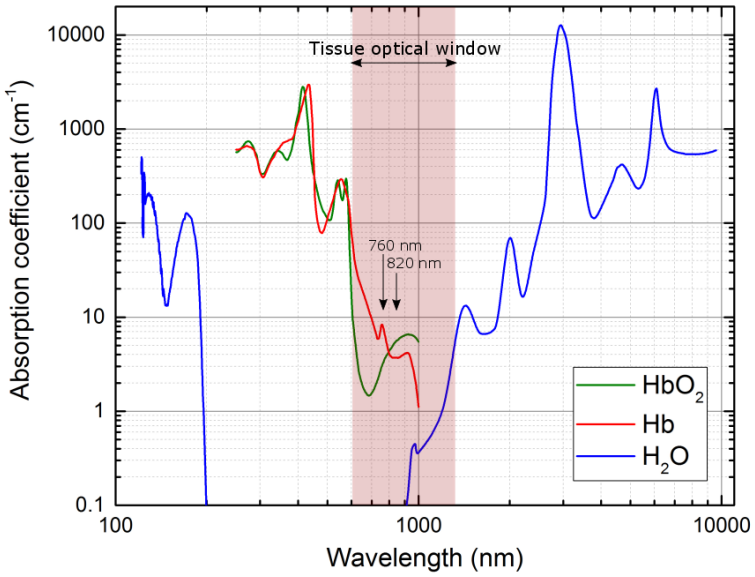

Figure 1: Light absorption by common absorbing tissue constituents. The tissue optical window is marked red and the, for this thesis, relevant wavelengths for oxygen and water vapor detection are marked by arrows. Data used in the figure is taken from S. Prahl [11] for hemoglobin and oxyhemoglobin, G. M. Hale and M. R. Querry [2] for water ($\lambda > 200$ nm) and K. Watanabe and M. Zelikoff [18] for water ($\lambda < 200$ nm).

3.2 Tissue types

The torso contains many tissue types and organs which are visible in a computer tomography (CT) image due to their difference in absorption of X-rays. CT is a common technique to map out components of the body by post processing of X-ray from multiple directions to create a cross section image. In figure 2, the tissue types important for this thesis is marked out on a CT image of a preterm baby girl born in gestational age of 33 weeks.

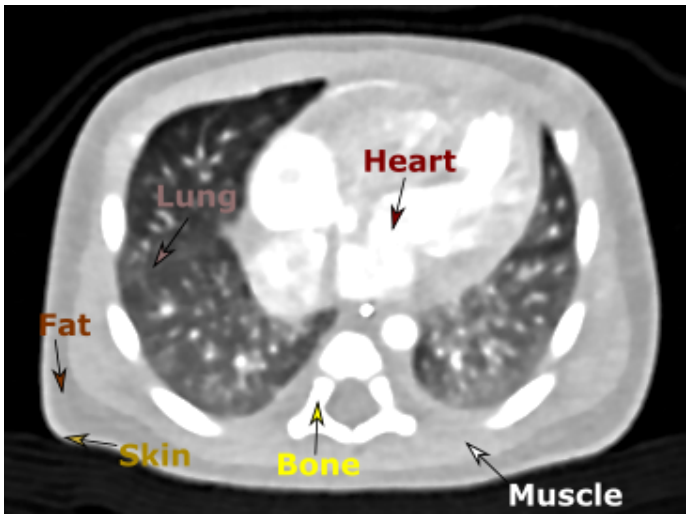

Figure 2: CT image as a cross section of a preterm baby torso. Heart, lung, fat, skin, bone and muscle are all tissue types marked in the image. The gray scale in the picture corresponds to the relative attenuation of X-rays starting from white as the most attenuation and black as the least. Lungs with mainly air content appears to be nearly black.

In addition to the attenuation of X-rays, the tissue types can be ordered by the different optical properties for wavelengths concerning this thesis work. Absorption coefficient and the reduced scattering coefficient for the tissue types are presented in table 1, the data is specific for light of wavelength 760 nm. The skin layer is excluded due to it being to thin for the model used in this thesis.

Tissue type	μ_a [cm^{-1}]	μ_s' [cm^{-1}]
Fat	0.1	11.5
Muscle	0.29	7.5
Heart	0.29	4.9
Bone (nylon)	0.2	46.5
Lung	air	air

Table 1: Tissue types and their optical properties at 760 nm. Data in the table is taken from [4].

4 Optical spectroscopy

4.1 Light absorption by gases

When light is absorbed by free atoms or molecules the transitions are quantized and only allows very specific wavelengths to be absorbed. This is the case for gases and gives rise to a narrow spectral lines. Solids and liquids differ from gases when absorbing light. The molecules are instead interconnected and will interfere with each other when light interacts with them. This leads to absorption of light over a broad spectrum, where the energy of the photons can be transferred to the material

over a continuous energy interval. The difference in absorption of gases in relation to liquids and solids is of great importance for this thesis work. Figure 3 depicts the energy levels of molecules, which are the specific levels for which energy can be transferred from and to photons. Atoms bonded together form molecules with electrons bound to energy states as shown as line A and X in the left diagram of figure 3. Molecules also have vibrational energies leading to an additional separation of molecular energy levels, as shown in the middle diagram of figure 3. When molecules are free in a gas, they also have rotational energy levels as in the right diagram of figure 3.

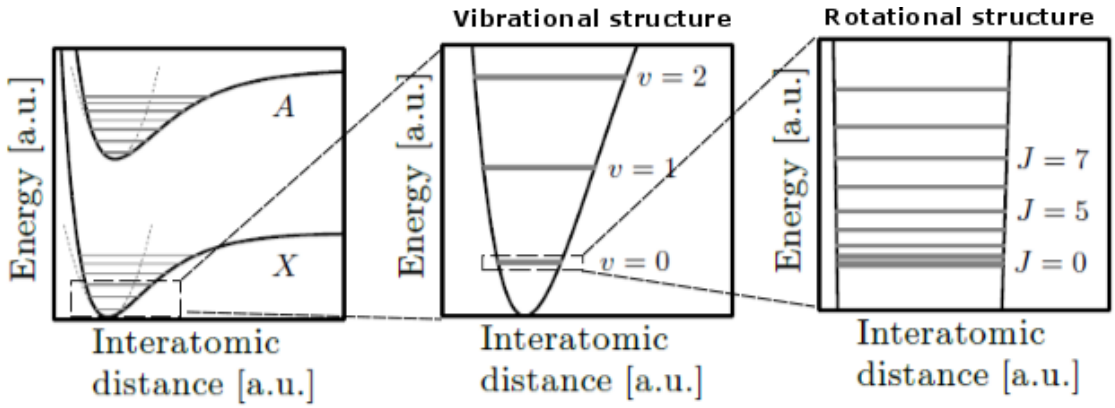

Figure 3: Molecular energy level diagram. The picture is used with permission and is modified from [6].

4.2 Line broadening

Spectral lines are not infinitely small but has a width due to broadening effects as is described in this section. Natural broadening is an effect following from Heisenberg's uncertainty principle which states that there is a minimum uncertainty for the product of energy and time. For example, the limited lifetime of a specific energy state, of an atom or of a molecule, will demand a larger uncertainty in energy for the transition. What until now was described by a very defined single wavelength absorption peak does now have a width, where more than one wavelength can be absorbed. For the natural broadening, this shape is described by a Lorentzian profile, which also can be seen in figure 4.

Doppler broadening is a result of the thermal motion of atoms and molecules when absorbing and emitting light. The observed light emitted from a molecule moving towards or away from the observer will be experienced as higher or lower frequency respectively, as is described by equation 4,

$$\nu = \nu_0(1 \pm \frac{v_r}{c}) \tag{4}$$

where ν is the frequency of the observed light, ν_0 is the center frequency for the transition, v_r is the velocity component and c is the speed of light. This broadening effect gives rise to a Doppler width, $\Delta\nu_D$, of the line shape expressed as,

$$\Delta\nu_D = \frac{\nu_0}{c}\sqrt{\frac{2k_BT}{M}} \tag{5}$$

where k_B is the Boltzmann constant, T the temperature and m the molecular mass. This results in a broadened Gaussian distributed line shape as shown in figure 4.

Pressure broadening comes from inter-molecular collisions where there is a disturbance in what photon energy that can be absorbed. This affects the effective lifetime of the excited state of the molecule which is reduced by collisions with other molecules. The magnitude of the effect depends on the gas pressure due to a higher probability for collisions at high pressures. Due to the natural distribution, pressure broadening generates a Lorentzian line shape just as the natural broadening.

The line shape of interest in this thesis work comes of course from a combination of the Lorentzian profile of pressure broadening and the Gaussian profile of Doppler broadening. Natural broadening is a minor effect and can be ignored.

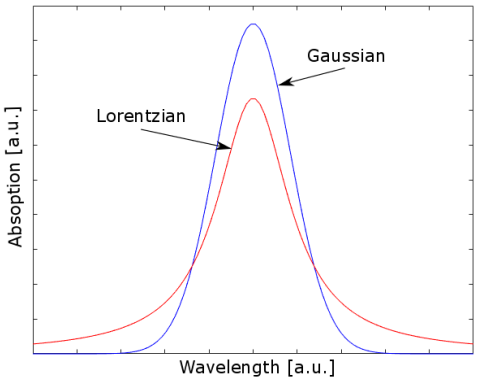

Figure 4: The Gaussian and Lorentzian line shapes as following the broadening of the spectral lines.

Tissue representation by liquid phantom

To simulate measurements on tissue, liquid phantoms can be constructed to have similar optical properties as the tissue that is being mimicked. For this thesis work, intralipid 20 % is used as the scattering agent and Rotring india ink is used as the absorber. Intralipid is mostly used as a parenteral nutrition and consists of small fat droplets suspended in water. It is well suited as a scattering agent for research purposes due to its high scattering coefficient and low absorption. It has also been proven to have good uniformity between batches and a variation close to 2 % [14]. India Ink is an absorber due to its insoluble carbon particles mixed in water. It is commonly used for tissue representation by liquid tissue phantoms but it has the drawback of not solely being an absorber, but also scatters due to its particles. Over time, the ink particles sink in the liquid and clusters together. According to P. Di Ninni *et el.* [10], it is therefore important to expose the ink to ultrasound for 30 minutes before using it. They also recorded large brand-to-brand and batch-to-batch variations for the intrinsic absorption coefficient, $\mu_{a,ink}$ and the intrinsic extinction coefficient $\mu_{e,ink}$, which in cases differed more than a factor of two. The albedo as the ratio $\mu_{a,ink}/\mu_{e,ink}$ only showed small variations. The absorption and scattering for each batch of india ink needs to be characterized before used.

5 GAs in Scattering Media Absorption Spectroscopy (GASMAS)

The spectroscopy used to measure light absorption by a gas enclosed by scattering media (GASMAS) is proven to be a very promising technique [8]. It is an extension of more general gas absorption spectroscopy techniques where the light travels an open path through a gas and with knowledge of the absorption pathlength within the gas, a gas concentration can be estimated. The gas of interest is not always with an open path with a well defined pathlength. GASMAS aims to measure gas concentration for gaseous cells surrounded by a scattering medium, where the pathlength can be defined from the absorption of light from a gas of known concentration within the same cell. The distance over which the light is being absorbed by the gas is for this thesis defined as the absorption pathlength, APL, even though this is not a conventional abbreviation. As for lung function monitoring, which is the topic of this thesis, it is of great importance to measure oxygen concentration in-vivo, non-intrusively and continuously to ensure that a preterm baby receives the correct breathing aid. When measuring gaseous oxygen within the body, there are some additional concerns that needs attention.

- Get enough light to reach the detector.
- The absorption signal should be calculated only from the gaseous cell of interest, not from absorption by bulk material or some other gaseous cell.
- The APL must be determined to get a quantitative value of the gas concentration.

The GASMAS technique has the possibility to solve these concerns, as presented in [6], [7] and [17].

5.1 Tunable Diode Laser Absorption Spectroscopy (TDLAS)

A diode laser is a compact, room-temperature operated source for monochromatic light. They are very suitable for absorption spectroscopy where the laser wavelength is scanned over an absorption line. When the wavelength matches that of the molecules resonance frequency, less light will be detected and a concentration of the specific molecule can be estimated.

In gas sensing using TDLAS, the laser wavelength is swept over the gas absorption line of interest by modulating the injection current to the diode laser. The current is ramped as a function of time where one ramping sequence include a wavelength change over the full absorption line. How to use current ramping is further described in section 5.2. In figure 5 the detected signal for a laser sweep over one O_2 absorption peak is shown by (a) direct absorption and (b) the absorbance after signal enhancement by digital post-processing. The absorption signal originates from the extinction of photons corresponding to the resonance frequency of the gas in relation to the extinction of photons of frequencies that are not absorbed by the gas. That difference in extinction is due to absorption and is determined by the amount of gas along the path of the light. The height of the absorption peak is therefore directly

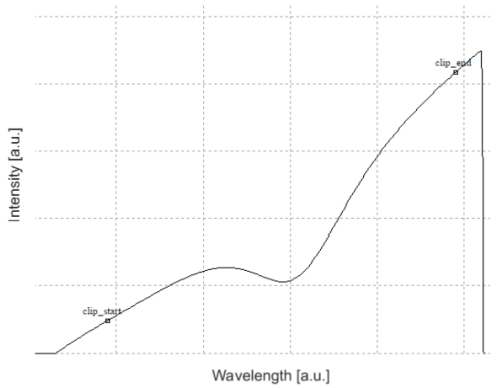

(a) Transmitted signal recorded by the detector. The direct absorption of gaseous oxygen is seen as a dip in transmitted signal. clip_start and clip_end denotes the data collection interval.

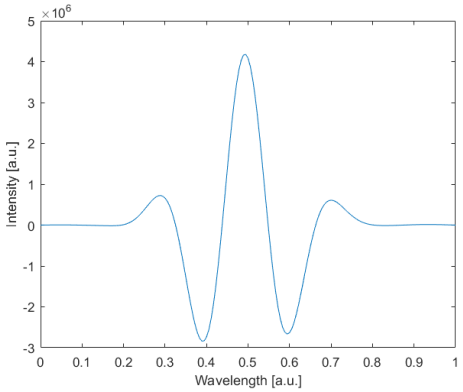

(b) Absorption peak after signal enhancement by digital post-processing.

Figure 5: Scan over a single O_2 absorption line close to 761 nm.

related to the the number density of absorbing molecules between the laser and the detector. The width is determined by the line broadening effects as described in section 4.2.

Scanning is done by modulating the current where the wavelength increases with increasing current. The attenuation of the incident light intensity, I_0 [W/cm^2], through the gas to the transmitted light intensity, I [W/cm^2], for wavelengths matching the molecular absorption line is expressed by Beer Lambert's law. The amount of light transmitted through the gas is dependent on the absorbing gas concentration, C [molecules/cm^3], and the pathlength, L [cm].

$$\begin{aligned} I(\lambda) &= I_0(\lambda)e^{-\sigma(\lambda)CL} \\ I(\lambda) &= I_0(\lambda)e^{-\mu_e(\lambda)L} \end{aligned} \tag{6}$$

σ [cm^2/molecule] is the absorption cross section of the absorbing molecule, which in turn depends on the wavelength, temperature and pressure. The second formulation of the equation uses the extinction coefficient, μ_e, as a measure of how much intensity decreases per length unit of scattering and absorbing media.

5.2 Laser diode wavelength tuning

Laser diodes are semiconductors with a set bandgap which is fully linked to the semiconductor material used. This bandgap is relatively fixed but can be slightly tuned with a change in temperature and injection current. A change in temperature affects the bandgap which in turn affect the wavelength of the light output. Higher temperature will result in an increased wavelength. A change in injection current will have impact on the effective cavity length of the laser diode. This is because of the refractive index change due to a new current density and instantaneously changed junction temperature.

5.3 Fundamentals of GASMAS

In GASMAS just as in TDLAS, the tunable diode laser is swept over an absorption line by modulation of the diode current. This sweep and basic absorption line can be seen in the two diagrams to the left of figure 6. The left picture also illustrates a simple gas cavity for TDLAS measurement where the pathlength, L, easily can be measured as the straight distance within the gas between the laser and the detector. But when performing GASMAS measurements, the turbid media surrounding the gaseous cavity will scatter the light, making it take a random path through the sample. The middle picture in figure 6 illustrates a GASMAS measurement of a large gas cell when two different beam paths through the same sample can result in different absorption signals, assuming that both of the beams are detected. The beam path avoiding the gas will only be absorbed partially by the bulk material. The beam traveling through the gas will, as well as the bulk absorption, also have an absorption signal very characteristic to the absorbing gas. The GASMAS measurement in the right picture of figure 6 also illustrates two paths with their different absorption signals, but here with small gaseous pores and detection on either side of the sample. The reason for this absorption signal to be smaller than the one in the larger cavity is due to the shorter distance traveled through the gas, and therefore less absorbed light of that particular wavelength.

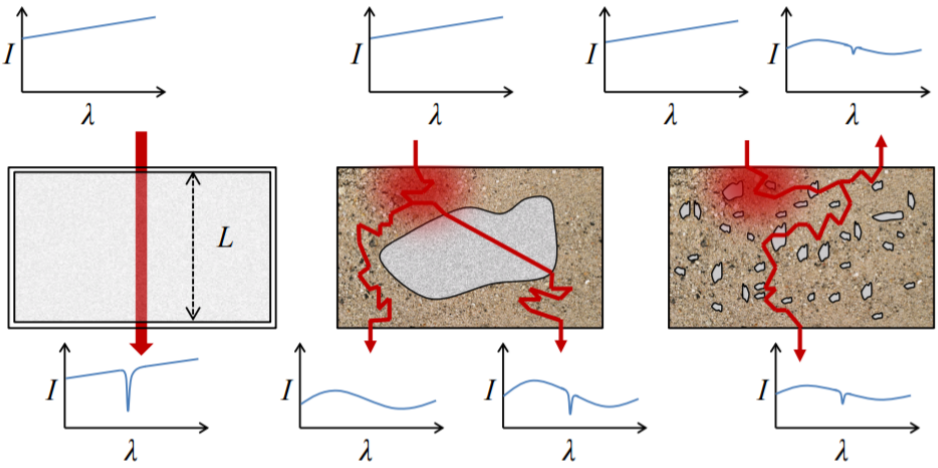

Figure 6: Schematics of absorption spectroscopy for different configurations of gaseous cavities. Left: TDLAS of a non-scattering gas cavity. Middle: A GASMAS measurement where one single large gas cavity is surrounded by scattering media. Right: A GASMAS measurement where multiple small gaseous pores are enclosed within scattering media. The picture is used with permission from [6].

5.4 Pathlength calibration

To calculate a gas concentration in a sample using Beer-Lambert's law (eq. 6), it is important to know the the length of the path, over which the light travels. It is in this path the molecular absorption occurs, which results in a transmission dip

relative to the total amount of absorption. If the sample is a non-scattering medium, the optical pathlength, OPL, is the distance between the light source and detector. For the GASMAS case, individual photon pathlengths are undefined due to the multiple scattering events of the light, resulting in a distribution of pathlengths within the gas. The average pathlength the light travels inside the gas is dependent of the scattering and absorption related to each wavelength.

For lung function monitoring, the gaseous oxygen in the lungs are of interest. The oxygen can easily be detected by analyzing the absorption of light at the absorption peaks close to 761 nm, but to quantify the concentration, a reference gas of known concentration needs to be measured. The lungs, with ever presence of water has a relative humidity 100 % which makes water vapor a suitable reference gas as its concentration can be calculated from knowledge of body temperature and gaseous pressure. Water vapour concentration, $C(H_2O)$ [molecules/m^3], can be calculated by equation 7,

$$C(H_2O) = \frac{p_s \cdot RH}{p_a \cdot 100} \tag{7}$$

where p_s [Pa] is the saturated water vapor pressure, p_a [Pa] is the atmospheric pressure and the relative humidity, RH, is the present air moisture in relation to maximum air moisture at this specific temperature and pressure.

The saturation water vapor pressure, p_s [Pa], is calculated by the equation presented by J.M. Richards [12]

$$\begin{aligned} p_s &= p_a e^{13.3185t - 1.9760t^2 - 0.6445t^3 - 0.1299t^4} \\ t &= 1 - T_{steam}/T \end{aligned} \tag{8}$$

Where $p_a = 101325$ Pa is the atmospheric pressure and T_{steam} is the steam temperature for water. As shown by L. Mei *et al.* [8], oxygen concentration is, due to assumed equal pathlength for both wavelengths, calculated with Beer-Lambert's law (eq. 6). The wavelengths 761 nm for oxygen and 820 nm for water vapour experience a similar absorption and scattering in the solid material, which can be explained by Mie theory. Thus, water vapour is a suitable reference gas for oxygen in the lungs.

Oxygen concentration in humid air

The oxygen concentration in normal ambient air is often considered to be 20.9 %. This is very close to the truth in non-humid air for normal atmospheric pressure. Much of the experiments in this thesis are of air with a relative humidity close to 100 % which results in less oxygen concentration as the water vapor molecules displaces the oxygen molecules. The oxygen concentration, $C(O_2)$, is calculated with eq. 9,

$$C(O_2) = C(O_2)_{dry} \cdot (100 - T_{corr} \cdot RH) \tag{9}$$

where dry air can hold $C(O_2)_{dry} = 20.95$ %, T_{corr} is the correction factor per temperature and is 0.04, 0.07 and 0.11 for 15°C, 25°C and 30°C respectively, RH is the relative humidity.

6 Method

The work of this thesis can be divided into two subcategories, where one is preparation, which includes setup of the laser system for optimized gas absorption to develop tissue phantoms for simulation of in-vivo lung measurements. The other is experimental, where the gas concentration is verified and GASMAS measurements are performed on the tissue phantoms as well as in-vivo on a newborn baby. The ambition for this thesis was to support GPX Medical in the development of a pre-prototype for GASMAS measurements and to use this system for all measurements. The pre-prototype was under permanent development through most of my thesis work and therefore another laser system was used for the measurements.

6.1 Laser system setup and calibration

The laser system is designed to measure molecular absorption for gaseous oxygen and water vapor using two lasers with wavelengths at 761 nm and 820 nm. The lasers are of distributed feedback, DFB, type and is supplied by Nanoplus [9]. The detector used is 10x10 mm with a silicon type photo diode from Hamamatsu [3]. Figure 7 illustrates how the laser can be tuned and how it is setup to scan the laser wavelength over a chosen absorption peak.

The laser wavelength scan is adjusted for the two laser diodes through temperature and current ramping as described in section 5.2. From the spectra in figure 7 it can be seen that the scanning range of the lasers are quite narrow. The experimental setup optimizes the scan so it is centered over the absorption peaks of interest with a high output power. As for the oxygen laser, the peaks are found for shorter wavelengths, which means it lases with low power because of the demand for low injection current to scan over the peaks. The output power from the laser is close to linearly proportional to the injection current for the lasers tested in this thesis. By lowering the temperature to its minimum, more current can be applied and more output power reached.

The line shape is calibrated, and relative transmission is measured and normalized to show 100 % when detecting all light. For the oxygen laser at about 761 nm, two peaks are measured and the result is an average of the two. The water vapor laser at about 820 nm only measures one peak due to no compatible set of two absorption peaks in the scanning range.

The measurement to verify the laser systems ability to estimate oxygen concentration was performed by measuring a well known oxygen concentration in air. 23 mm laser to detector distances in the interval 5 mm to 150 mm was measured. The air oxygen concentration is 20.9 %, the ambient pressure, $p_a = 1019$ mBar at a temperature of $T = 23.3$°C.

6.2 Tissue phantom development

To simulate GASMAS measurements on an infant, realistic tissue phantoms are produced. These have a geometry resembling that of air-filled lungs within layers of

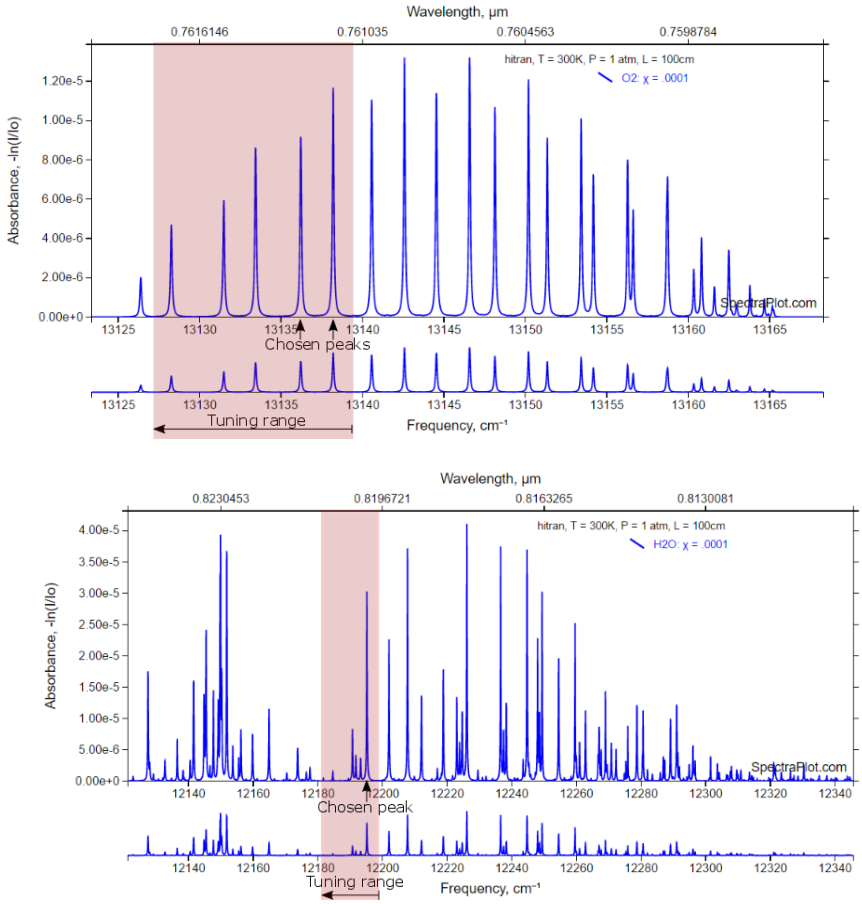

Figure 7: Absorption spectra close to laser wavelength. Maximum tuning range of laser diode and chosen absorption peaks for measurements are marked out. Spectrum generated by SpectraCalc. These scanning ranges and the chosen peaks are applicable to the pre-prototype being developed. They are not directly transferable to the laser system used for the actual measurements in this thesis. The top figure shows the absorption spectrum for oxygen close to 760 nm. The bottom figure shows the absorption spectrum for water vapor close to 820 nm.

tissue-like liquid. The method to obtain phantoms of optical properties similar to that of the tissue types described in section 3.2 is to 3D-print anatomical phantoms to be filled with phantom liquid prepaired as in table 4.2. Two models have been developed and will be further described later in this section. The models described in this section are developed from .Stl data files and 3D printed with the help of Olaf Diegel and Jonny Nyman at IKDC in Lund, using an 3D printer of model EOS Formiga P110 selective Laser sintering system. The material used is white nylon with absorption coefficient of 0.02 cm^{-1} and reduced scattering coefficient of 46.5 cm^{-1} as can be seen in table 4.2 in section 3.2.

Simplified model of lungs within tissue

The most simple model used in this thesis work to simulate lungs within tissue is that of two 3D printed slabs filled with liquid tissue phantom to resemble human tissue, separated by air as to resemble lungs. The geometry for measurements are

shown in figure 8 where light, after scattering around in the first slab travels a distance L in air, acquiring an oxygen absorption footprint, to continue scattering within the second slab before reaching the detector.

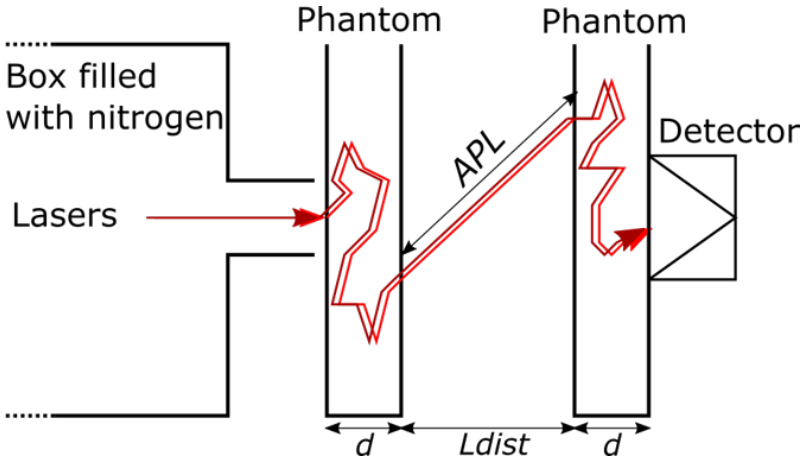

Figure 8: Experimental setup to measure oxygen concentration in the air in between two slabs filled with a liquid phantom. d is the slab thickness, $Ldist$ is the distance between the two tissue slabs and APL is the average absorption pathlength for the light.

When calculating the pathlength for the light with a wavelength of 820 nm for water vapor, the absolute concentration of water vapor in the air need to be known. Even though the relative humidity in the ambient air can be measured with high accuracy, the humidity between the slabs is varying due to the "sweating" of the slabs. The humidity is highest at the bottom between the slabs where it was estimated to around 20 percentage points (pp) above the ambient humidity. For this reason, the uncertainty of the measurements are mostly determined by the uncertainty of water vapor concentration in the air and is therefore considered unusable until a more stable environment can be obtained. Two solutions to the controlled environment problem were proposed where one is sufficient ventilation by circulating the air close to the experiment by a mini fan. The second solution, and the solution used for the following measurements is enclosement of the whole measurement setup by a plastic bag with water present to ensure 100 % humidity. This gave best results and is simple to apply.

Life size 3D printed model of an infant

For a more realistic simulation of lung gas measurements in a preterm baby, an ergonomically 3D printed model of an infant was made. This model is a further developed version of a model used by Jim Larsson [4] and Peilang Liao [5]. The procedure is similar to the one described in [5], where the model is constructed from 137 CT-scan images of the torso of a preterm baby, thirteen days after its birth at a gestational age of 33 weeks with a weight of 1.7 kg. New for the model developed for this thesis is the extra effort put on creating the model more ergonomically correct by using a different set of 3D programs. The final model used for measurement geometry experiment is shown in figure 9.

Figure 9: The 3D printed model of a prematurely born baby torso used for realistic measurements of oxygen concentration in the lungs. From the left is an outer body, hollow, to be filled with fat and muscle phantom, bone structure, solid, lungs, hollow, containing air and the heart, hollow, to be filled with heart muscle phantom.

The model in figure 9 consists of a heart (right), which is hollow and will be filled with heart tissue phantom. The lungs (second from right) are hollow and contains air of 100 % humidity. The bones (second from left) are 3D printed solid and made of nylon material. The torso (left) is hollow and making up two layers, where the outer layer is to be filled with fat tissue phantom and the inner layer is to be filled with muscle tissue phantom. The properties of the liquids to be filled in the model can be found in table 1.

The procedure to create the model starts by importing the 137 CT-scan images, provided by Lund University Hospital, into the medical image program 3D Slicer [13]. A screen view of the program is shown in figure 10. With this program it is possible to separate different tissue types from each other by a segmentation tool which distinguishes between different extinction of X-ray radiation. The groundwork for the segmentation is already made by Peilang Liao [5], thereafter, with support of the Slicer segmentation tool, the markups are updated to more accurately represent reality and also to strengthen what earlier have been weak parts of the model. With the segmentation for all the tissue types at all pictures, Slicer can be used to generate a 3D model of each of the organs separately which is saved as stl format.

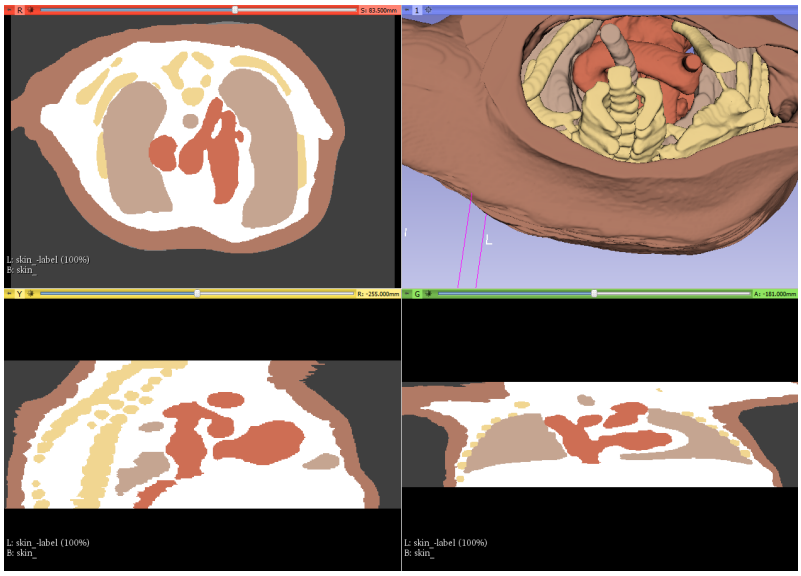

Figure 10: Slicer master view during tissue type markup. The proportion of the model is yet to be corrected.

The generated 3D models are then imported to the 3D program Meshmixer for the final modifications. In this program the proportions can be changed for the model to have correct size. This can be done since the voxel dimensions from the CT-scan is known to be 0.246094x0.246094x0.7 mm^3. In this program the model is further modified to strengthen weak parts, i.e. the windpipes and bones. The last step in the model creation is to apply smoothing to all surfaces and fill in the bone for it to be solid and making the other organs hollow.

Improvements involve smoothing of the surfaces, which simplifies measurements by enabling the laser and detector to come closer to the surface, with less air pockets. It also makes it possible to use thinner wall thickness of the model when 3D-printing. The bottom plate is updated as being a transparent plastic disc to which the model is glued stuck with a silicon sealant. This way the leakage of the filled model is minimized to only a couple of cl per hour.

What has not been accounted for in this 3D-model of the infant is the inside structure of the lungs. It is in this thesis assumed to be air filled which is true to some extent. From the segmentation process, a screen shot of the lungs was taken from 3D Slicer and is shown in figure 11. The lungs are enhanced and are clearly visible in the center of the picture.

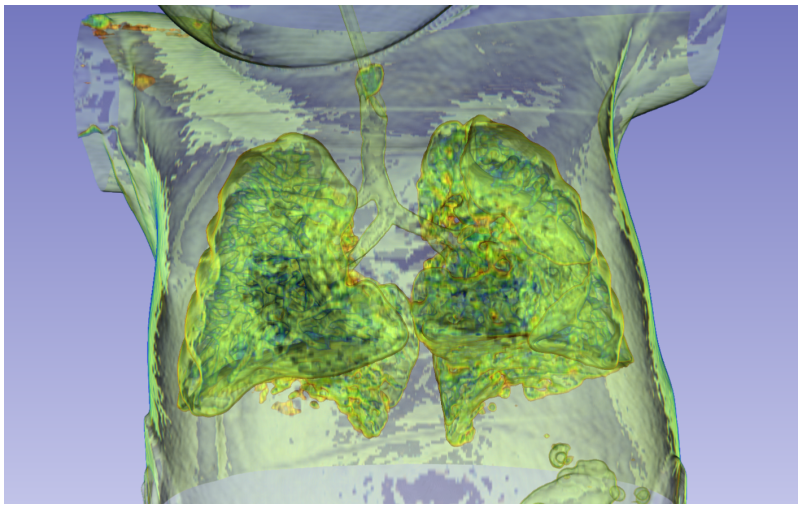

Figure 11: A contrast enhancement of the lungs of the same infant as the one being 3D-printed as a model. The lung structure is clearly not solely an air filled cavity. What also can be seen is the bronchial passages.

Absorption coefficient calibration

For this thesis work, Rotring India ink is used as the absorber and its absorption properties is evaluated through a collimated transmittance measurement. The schematics of the implemented experimental setup in figure 12 shows how the collimated laser light passes through a cuvette of length L=10 mm, continues towards the detector and due to the pinholes only measures the ballistic, unscattered, light. The acceptance angle for the collimated light is $\theta \leq 1^{\circ}$. The technique is based on a comparison between a sample of disinfected water, representing a low absorbing media, with a sample of ink dissolved in water. The absorption of the ballistic photons are described as a function of ink density in the water. The intensity through the water sample is the reference, $I_0(\lambda)$. The transmitted intensity through the ink and water mixture is denoted $I_s(\lambda)$. The extinction coefficient, μ_e (eq. 2), is calculated by Beer Lambert's law (eq. 6). Pathlength difference in the sample is negligible due to the almost identical refractive index.

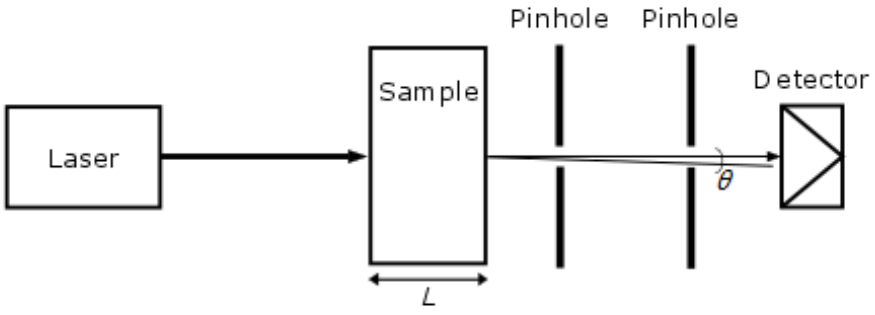

Figure 12: Experimental setup for collimated transmittance measurements to determine absorption coefficient of Rotring India ink. L is the cuvette width and θ is the acceptance angle.

For the ink to be well mixed into the water, it is important to apply ultrasound to the solution [10]. Due to the evaporation of water when applying ultrasound to the cuvette directly, it is deemed sufficient to apply ultrasound to a sealed batch of ink densely mixed with water prior to mixing the final diluted ink mixture.

By measuring the extinction coefficient for multiple ink concentrations, the absorption coefficient was determined to be 5748±72 cm^{-1} for this particular batch of ink.

Optical characteristics of mixed tissue phantom

Photon Time of Flight, PToF, is a common approach for evaluating optical properties in highly scattering media. It is a measurement technique where the temporal broadening of multiple short light pulses are evaluated when the light travels through a scattering media. Figure 13 shows the setup of the laser and detector fiber inserted into the liquid, the fibers are placed so that the sample can be approximated as an infinite medium.

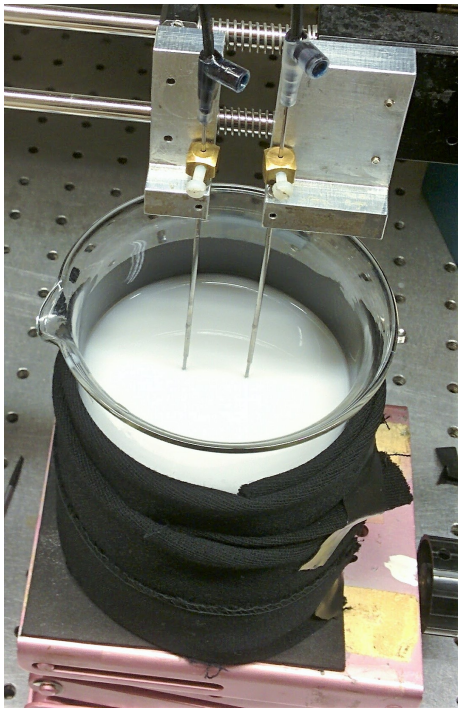

Figure 13: Setup for PToF measurement of a highly scattering intralipid and water mixture. The separation between the laser and detector fibre is well measured to 20 mm.

A mixture of 500 ml was prepared containing 18.5 ml intralipid, 2.5 ml ink (1:100 diluted in water) and 479 ml water. The scattering and absorption of the phantom mixture is analyzed to verify the optical similarity to tissue. The tested mixture is made to have similar optical properties as muscle tissue. The acquired optical properties from PToF for 761 nm and 820 nm is shown in table 2. The ink is assumed to be the sole absorber and the intralipid as the sole scattering agent.

λ [nm]	$\mu_{a,ink}$ [cm^{-1}]	$\mu'_{s,il}$ [cm^{-1}]
761	6800	212
820	5440	185

Table 2: Optical properties measured with a PToF system of a close to infinite medium of laser and detector fiber spatially separated by 20 mm well inside a glass of 500 ml liquid. Ink is considered the only absorber and intralipid is considered the only scattering agent.

6.3 GASMAS tissue phantom measurements

For the experiments, the GAS PI1 system at Gasporox [1] was used, which yields an output power P_{O_2} =1.2 mW and P_{H_2O} =1.5 mW at the absorption peaks predetermined by the system. Because of the relatively weak signal strength, a long exposure time has been used for all experiments with the 3D printed models. The intended laser power for the pre-prototype, which is being built alongside these experiments, are approximately 50 times stronger. To compensate for the lower laser power, an average of 50 rampings have been used to get reliable measurements.

GASMAS on simplified lung model

Two experiments are performed using the slabs. One using slabs of the fixed thickness $d = 6$ mm, and measuring the absorption signal of both lasers for 15 different *Ldist* between 15 mm and 50 mm. A schematic picture of the measurement geometry is shown in section 6.2 figure 8. This is to investigate how the system estimates oxygen concentration depending on how long pathlength the light travels in the lungs. The other experiment is done with a fixed distance between the slabs $Ldist = 30$ mm with different slab thicknesses, $d = [4\ 6\ 8\ 10\ 12]$ mm.

The liquid tissue phantom used in the slabs has similar optical properties as muscle tissue as shown in figure 1. Due to some slight "sweating" of the slabs, the air between the two slabs have varying humidity which is highest at their mid base and lower close to the edges. To control the environment, knowing the air pressure, air temperature and especially air humidity, is paramount for quantitative estimation of the oxygen concentration in the air. By using a fan to circulate the air between the slabs, ambient air conditions are nearly reached. To create an even more accurately controlled environment, the setup was enclosed in a plastic bag with 99.9 % humidity. The laser and detector were outside the plastic bag in direct contact with the bag and slabs without any visible air pockets in between.

In these experiments, by letting the light travel an unknown pathlength in humid air, the method of using water vapor for pathlength calibration is tested. Pathlength differences between the 761 nm and the 820 nm laser were evaluated.

GASMAS on infant model

Determination of an optimized measurement geometry for gas measurements in the lungs is performed by tests on the 3D-printed infant model. The laser and detec-

Geometry	Laser position	Detector position
1	Back left	Chest left high
2	Back left	Chest left low
3	Side left	Chest left high
4	Side left	Chest left low
5	Side left	Side right

Table 3: Measurement geometries for the initial evaluation.

tor positions for the initial geometries are described in table 3. The liquid tissue phantom used is mixed to resemble the optical properties shown in table 1. They have been accurately measured according to the recipe and procedure described in section 6.2. This is by using the result from the photon time of flight measurements for optical properties of the mixed tissue phantom. Even though small variations can occur each time the tissue phantom is mixed, it is considered small and is not accounted for in this thesis.

Of all the tested geometries, only test 3 and 4 yielded a strong enough absorption amplitude with a desired curve shape for the two laser wavelengths. These positions were therefore more thoroughly investigated. A total of 12 detector positions and one laser position is tested further. Only one laser position could be used because of the bulkiness of the laser head, which only allowed one position of good contact with the model at the side of the body, under the armpit.

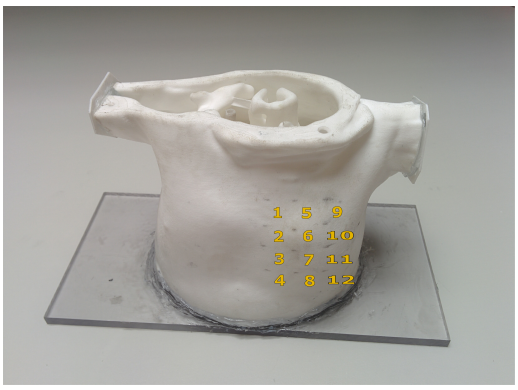

(a) Detector positions tested for signal amplitude evaluation and oxygen concentration estimation.

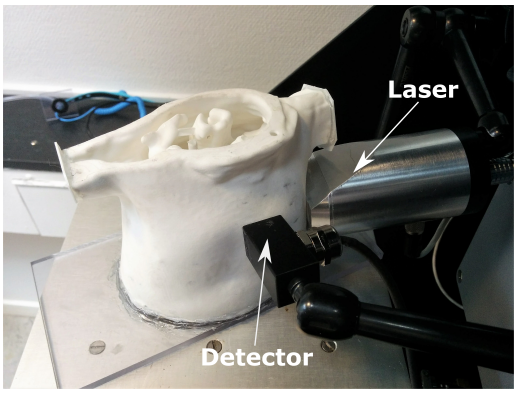

(b) Setup for measurement of oxygen concentration in the lungs of the infant model. The infant model is in this picture not filled with liquid tissue phantom.

Figure 14

Because of a large laser head and detector, it is difficult to avoid air pockets outside of the infant model both on the laser and detector side. To minimize the effect of unwanted absorption signal, a small nitrogen filled transparent plastic bag have been put on the contact surface of the model to fill a maximum of a few mm with nitrogen instead of air. For some tests, this largely reduces the absorption signal that is scattered back and forth between the sight source and detector.

6.4 In-vivo measurements on a three week old baby

As it is the goal of this thesis to improve and verify the quality of measurements to determine oxygen concentration in the lungs of preterm babies, I have been given a great opportunity to do measurements on a three-week old baby (not preterm). Though this is a healthy baby, much larger than those the final system is aimed to monitor at a neonatal clinic. This measurement series have provided invaluable input about what is required for the real life measurements. The father and mother of the baby are largely involved in the Neo-lung project and have been part of all measurements described in this section.

The system used is GAS PI1 as in all phantom measurements earlier described in this thesis. Acquisition of data was set to 5 ramping sequences for averaging, and in some cases which, along with the presented result, will be specified to be 10 ramping sequences. Each ramping sequence has a one second duration and the acquisition time chosen is a compromise between what is required of the system to provide a reliable result and the fact that it is difficult to preform long time measurements due to the movement of the baby.

First a series of reference measurements were made. Measuring through styrofoam for acquiring a good signal as a best possible reference. Measurement through an adult forearm to ensure no absorption signal is detected when no gaseous oxygen is present. Measurement on an air filled adult cheek to verify a signal curve shape as expected.

Measurements have been done with the baby sleeping in the arms of the mother. More than 20 measurements were performed on the sleeping baby and much time and effort was spent on finding geometries which resulted in a good signal. How it looked like when measuring with a chest to armpit geometry is shown in figure 15.

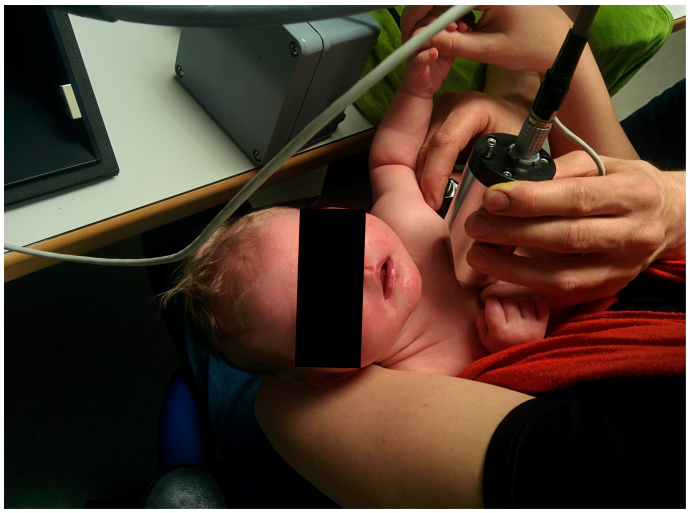

Figure 15: In-vivo measurement of the three week old baby.

Due to the difficulty to record a stable signal, much data was rejected directly. The main geometries tested are stated in table 4. All the three geometries were tested more than once with slight variations in position.

Geometry	Laser position	Detector position
1	Chest left	Armpit left
2	Chest left	Chest left
3	Stomach	Stomach

Table 4: Measurement geometries evaluated during for in-vivo tests.

Due to difficulties getting reliable quantitative measurements of oxygen concentration in the lungs, extra effort has been made for this section to save the signal curve shape for the measurements to be used for comparative signal-to-noise ratio, SNR, estimations. The procedure on how to estimate SNR is described in the next section 6.5.

6.5 Signal-to-noise ratio estimation

The absorption signal curve is fitted with an ideal signal curve and the quality of the fit is used to estimate a Signal to Noise Ratio, SNR. The ideal curve is acquired from a measurement using the same system and setup but measuring a long absorption pathlength with high transmission. The curve fitting is performed according to the Levenberg-Marquardt method for non-linear least square curve fitting. Figure 16 shows the signal curve and its fitted curve in comparison to the ideal curve shape. The SNR is defined as,

$$SNR = \frac{Signal\,peak}{Std(Signal - Fitted\,signal)} \tag{10}$$

For this thesis, the signal used for SNR estimation has already gone through a post-processing where it is enhanced. It could be argued that a second derivative or raw signal should be used instead for SNR calculation, because those would be less processed by the software. Most important is that SNR can be quantified and compared between measurements.

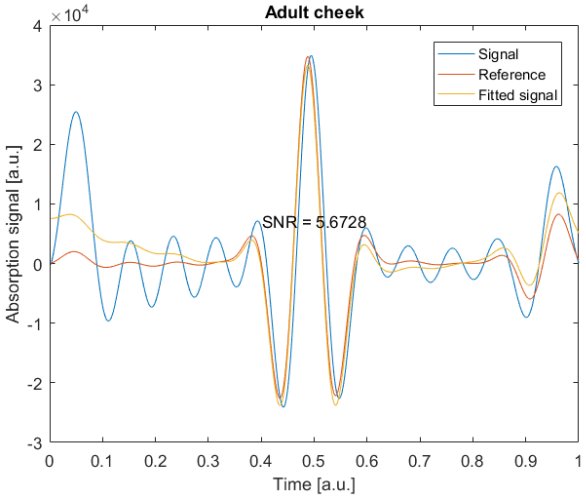

Figure 16: Water vapor measurement in an adult cheek. The measured signal (blue) is fitted to the reference signal (red) by Levenberg-Marquardt method for non-linear least square curve fitting. The curve fit is drawn as the yellow line in the figure and the SNR is calculated to 5.7.

7 Results and discussion

7.1 Laser system setup and calibration

The GASMAS system used for the measurements in this thesis is the GAS PI1 system at Gasporox. It is a product built to measure oxygen and water vapor concentration in the head space of milk and juice like packages which are made out of paper. Because it is a ready product, the settings need to be adjusted to these specific measurements. The measurements are also validated in this section where a known atmosphere, that is ambient air, is analyzed.

The laser system is intended to use knowledge of the known concentration of water vapor to calculate an absorption pathlength, APL, for the light to be used for oxygen concentration estimation. Since the composition of the atmosphere is known in air, an inverted measurement is conducted, where both the 761 nm and 820 nm lasers are used separately to estimate the real distance between the laser and the detector. The experiment consisted of 23 laser to detector distances to be estimated by the two lasers. The experiment distances was in the interval 4 to 152 mm. Logarithmic axes are often used to enhance the results for small absorption signals. The plot in the top of figure 17a shows the estimated distance by the two lasers. The x-axis gives the real pathlength measured with a caliper. The bottom left graph shows the relative distance estimation difference for the two lasers. The right graph shows the linear regression, which gives a value of the correlation between the two estimations. Values close to 1 indicate full correlation, which is to be expected when measuring the same distance with two different lasers.

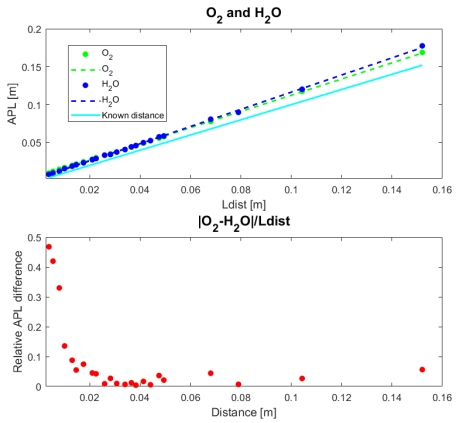

(a) Top figure shown an estimation of a known distance with the 761 nm and 820 nm laser separately. Bottom is the relative difference in distance estimated by the two lasers.

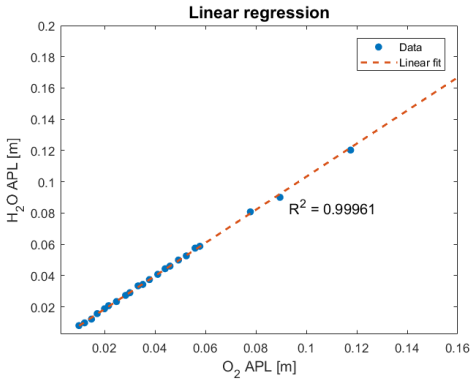

(b) Linear regression of the APL measured by the 761 nm and 820 nm laser.

Figure 17: Absolute distance is the signal, in [%m], multiplied by the known gas concentration in air. For distance calculation by the 820 nm laser, water vapor concentration is approximated as described in section 5.4 which considers ambient pressure, temperature and RH.

The result in figure 17b shows good correlation between the two wavelengths. They behave similarly when estimating many different distances. But the absolute distance estimation in the top of figure 17a reveals a overestimation of the distance in comparison to the actual distance for the two wavelengths. This is assumed to be an instrumental offset due to air in the laser head, resulting in an extra absorption signal induced before the light leaves the laser head. This offset signal does not significantly affect how the system estimates oxygen concentration due to a constant similar error for both lasers. The APL estimated by the lasers is relatively large for short distances. A hypothesis before these experiments was that the absolute error of the measurements would be constant, regardless of distance between the laser and the detector. This assumes however that the statistical errors of the measurements and distance calculations are independent of gas absorption magnitude. This could explain the large relative APL difference between the two wavelengths for short distances, just by the fact that the statistical errors in the estimations are more apparent for short distances. Noteworthy is that, for long distances, the relative APL differences do not converge to zero. This needs to be further investigated, but it is possible that the system not is sensitive enough for low light transmission measurements. Further on, the problem of a small absorption signal or low transmission of light will be discussed. In this experiment, the detected power for the two lasers separately spans from around 0.2 mW for the shortest distance to 0.6 μW for the longest distance tested.

To show how well the oxygen concentration is estimated by the system, the data from figure 17 is presented anew in figure 18, but now with the aim to compare two estimation methods. The known oxygen concentration, cyan colored line, is compared with the approximations where the APL is extracted from the 820 nm experiments, blue line, or when APL is taken from the caliper measurements, red line. The relative error is how much different the two wavelengths estimate distance

in relation to the caliper measurements.

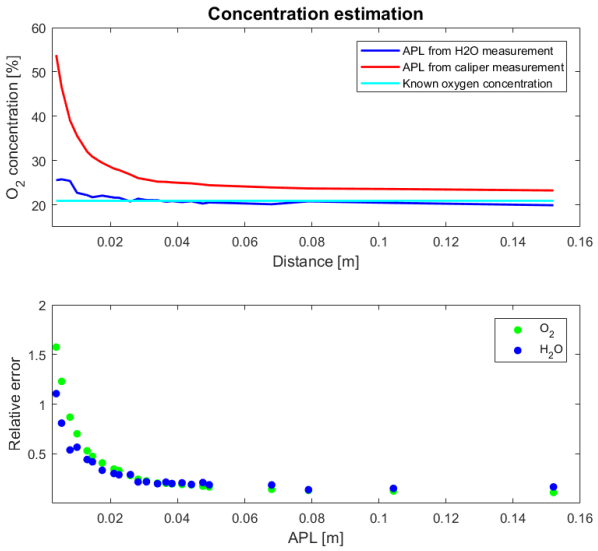

Figure 18: The top figure shows oxygen concentration estimated by two different methods, both compared to the known oxygen concentration in air. The bottom figure shows the relative error for the two laser measurements when estimating distance, in relation to the distance measured by the caliper.

It is clear form the red line in figure 18 that a large error is present which is more apparent for short distances. This is thought to come from the instrumental offset which gives a constant extra absorption signal for both lasers. 761 nm light travels a longer distance in air than the one measured by the caliper resulting in an over estimated concentration in air. The 820 nm laser measurement will be affected equally by the instrumental offset, and thus it gives reliable estimation of the oxygen concentration over a sufficient distance. How the offset affects the relative error can be seen in the bottom picture of figure 18, which further underline the large error for distances shorter than 1.5 cm.

To compensate for the instrumental offset, a linear fit is applied on the two data sets in top figure 17a and an extrapolation to zero distance is made. This resulted in an instrumental offset of 5.5 mm for both wavelengths.

After applying the instrumental offset of 5.5 mm, the distance estimations by the two wavelengths correlate much better with the distance measured with the caliper as is shown in figure 19a. For distances shorter than 1.5 cm, the accuracy is still fairly low. The correlation between the two wavelengths is approximately the same as the correlation for the data with an offset. The slight difference depends on the water vapor calculation inside the instrument, which is the only altered factor. This change of correlation from $R^2 = 0.99961$ to $R^2 = 0.99962$ is insignificant.

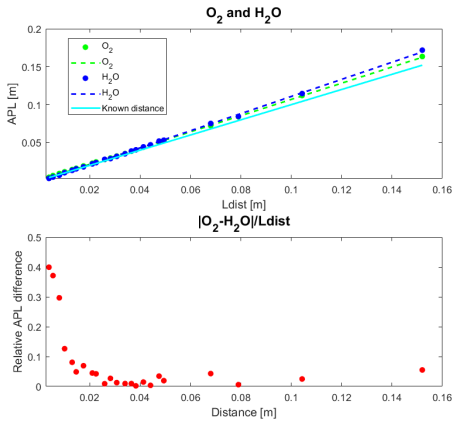

(a) Top figure show absorption pathlength by measuring O_2 with the 761 nm and H_2O with the 820 nm laser separately. Bottom is the relative difference in distance estimated by the two lasers.

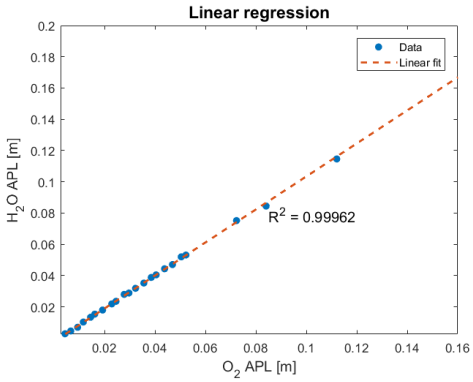

(b) Linear regression of the absorption pathlength measured by the 761 nm and 820 nm laser.

Figure 19: Absorption pathlength is the signal, in [%m], multiplied by the known gas concentration in air.

Figure 20 shows the calculated oxygen concentration, using two estimation methods. Compared to figure 18, the instrumental offset is here accounted for. It is clear that the offset adjustment has resulted in an estimation that better agree with the actual distance (figure 20). The estimate, using the APL from the caliper is greatly improved. For the actual application of measuring an unknown oxygen concentration in the lungs, a caliper can not be used for measuring pathlength in the lungs, but this test is a good verification of the system. Evaluation of the oxygen concentration using the H2O absorption pathlength is practically unaffected by the offset correction (figure 20). It shows very good estimates for $Ldist$ larger than 1.5 cm where the average oxygen concentration is estimated to 20.9 $\pm$ 0.652 %.

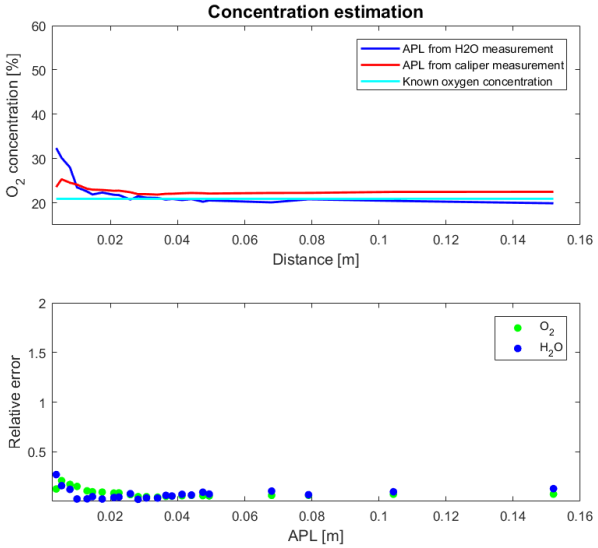

Figure 20: The top figure shows oxygen concentration estimated by the two different methods, both compared to the known oxygen concentration in air. The bottom figure shows the relative error for the two laser measurements when estimating distance, in relation to the distance measured by the caliper.

An important observation is that oxygen concentrations calculated using the caliper as an estimation of the APL always overestimate the known concentration, even for increasing measurement distances. The reason for this is not clear. The caliper always measures the shortest possible APL between the laser and detector. This experiment was conducted in free space where the light, can possible take a longer path by hitting reflecting surfaces in the room and anyway reach the detector. Also ambient light with more absorption magnitude can reach the detector, which would result in a bad estimation by using caliper as an APL measurement. Both of these effects will lead to a higher absorption magnitude detected than the one of the light going the intended path. It is important for the system that the 761 nm and 820 nm laser behave in a similar manner. If both lasers take a longer path than expected through the gas, the oxygen concentration estimate will still be accurate.

The absorption magnitude is shown as the histogram in figure 21. The green bars are for 761 nm laser absorption magnitude and the blue bars are for 820 nm laser absorption magnitude. The line plots shows the detected power where green line is for the 761 nm laser and blue line is for the 820 nm laser.

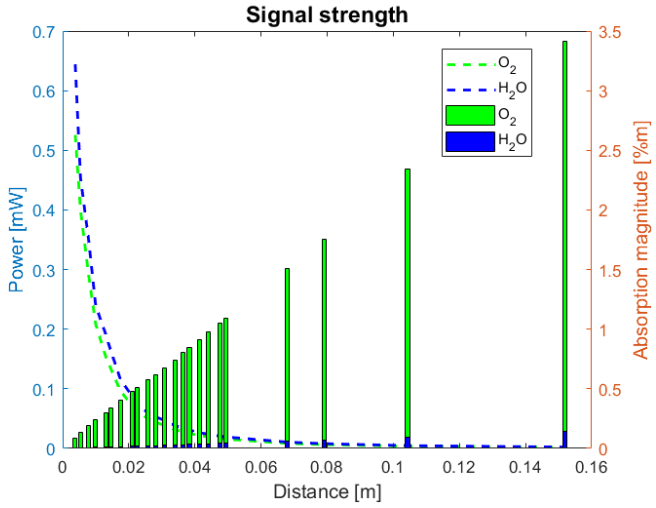

Figure 21: The histogram shows the absorption magnitude as a function of laser to detector distance. The green bars are oxygen and blue bars are water vapor. The line plot shows the detected power as a function of laser to detector distance.

The absorption magnitude for both laser wavelengths increase linearly with distance while the power drops exponentially. Oxygen gave a higher absorption magnitude than water vapor which is easily explained by the higher amount of oxygen in the air. With the current conditions, the air contained 20.9 % oxygen and water vapor only 0.9 % as calculated by eq. 7 and 9.

7.2 GASMAS tissue phantom measurements

The following chapter treats results related to the main objective of this thesis, namely to develop and use a model to simulate measurements of a real living preterm baby. The results from the simulations will be presented, first on a simplified lung model as shown in figure 8 and then on to measurement geometry optimization on the anatomical model in figure 9. The experiments are described in detail in section 6.3.

GASMAS on a simplified lung model

Two 3D-printed slabs are filled with liquid tissue phantom to resemble human tissue, separated by air as to resemble lungs (figure 8). The measurement results in figure 22 show how the two laser wavelengths estimate the pathlength between the two filled slabs. This is a known atmosphere of 99.9 % relative humidity and the results are therefore comparable with each other. The 761 nm light and the 820 nm light experience absorption signal from different pathlengths, which is reflected by the separation of the lines in figure 22a. The relative APL difference, about 20 %, is insufficient for accurate measurements. This difference has no effect on the correlation which can be seen to be close to 1 in figure 22b.

To compensate for the uncorrelated lasers, an assumption was made that the difference in scattering and absorption between the two laser wavelengths results in an

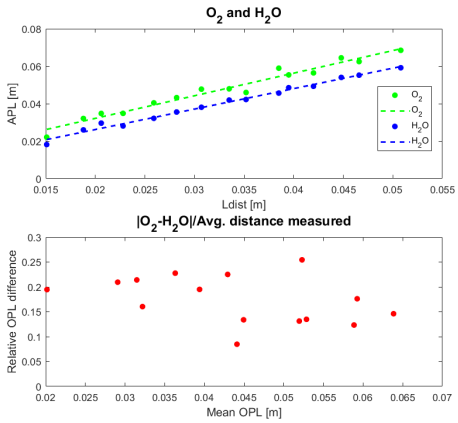

(a) Top figure shown an estimation of a know distance with the 761 nm and 820 nm laser separately. Bottom is the relative difference in distance estimated by the two lasers.

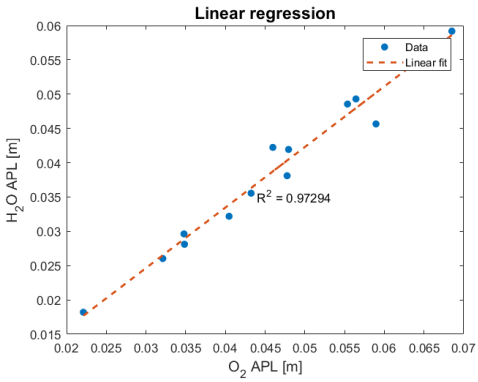

(b) Linear regression of the absorption pathlength measured by the 761 nm and 820 nm laser.

Figure 22: Measurement through slabs of thickness $d = 6$ mm for different *Ldist* to simulate the tissue-lung-tissue geometry.

APL difference that can not be ignored. According to Rayleigh and Mie scattering theory, the scattering for 761 nm light is greater than the scattering for 820 nm light. That leads to a greater possibility for the 761 nm laser to scatter further out in the slabs to take a longer path in air before it reaches the detector. Multiplying the absorption pathlength measured by the 820 nm for water vapor by a factor of 1.2 gives the results shown in figure 23. The correlation is still very good and the relative APL difference is below 10 % which is considered acceptable in this work.

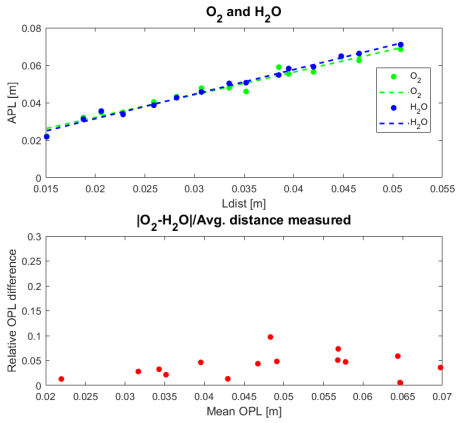

(a) Top figure shown an estimation of a know distance with the 761 nm and 820 nm laser separately. Bottom is the relative difference in distance estimated by the two lasers.

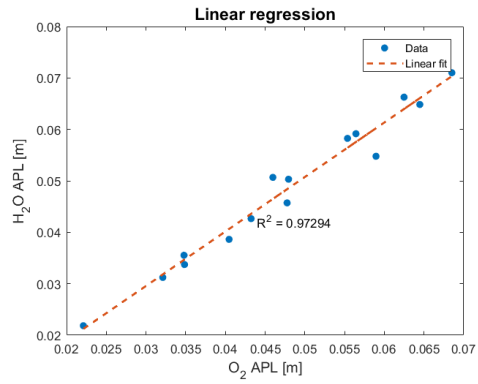

(b) Linear regression of the absorption pathlength measured by the 761 nm and 820 nm laser.

Figure 23: Measurement through slabs of thickness $d = 6$ mm for different *Ldist* to simulate tissue-lung-tissue geometry.

Although the factor of 1.2 is determined based a rather small data set and for now lacks confirmation by additional experimental observations, it seem to adjust for the problems concerning the APL difference in figure 22. I have chosen to call

this correction for the APL difference factor which is equal to 1.2 for this specific measurement geometry. Important to note is that for all further experiments, this correction factor will be used.

The oxygen concentration in the air between the two slabs were estimated and the result is shown in figure 24. The results vary from 19 % to 22.5 % and measures an average concentration $C_{O_2} = 20.67$ %, very close to the known concentration of 20.8 % in room tempered humid air.

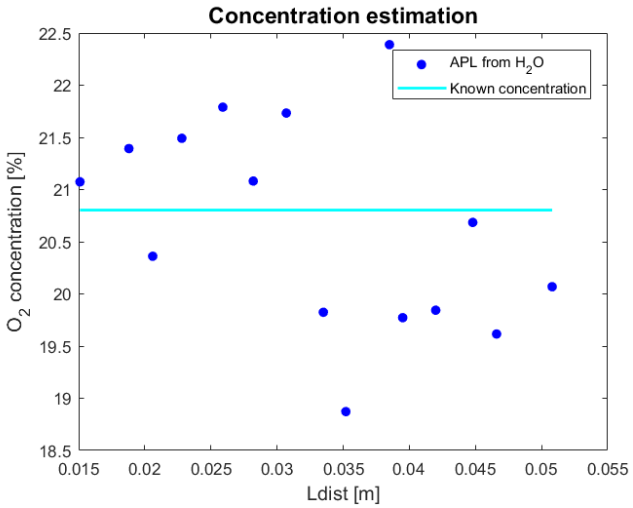

Figure 24: Oxygen concentration estimated for the humid air in the simplified lung model.

Figure 25 illustrates how the absorption magnitude and transmitted power as a function of the spacing between the filled slabs.

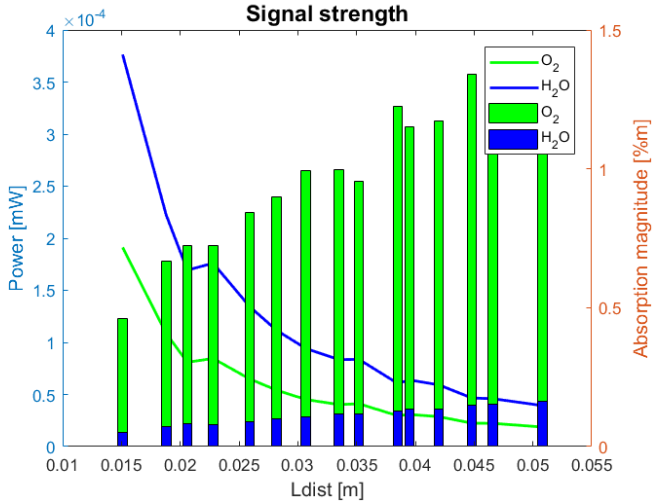

Figure 25: The bar plot shows the absorption magnitude as a function of *Ldist*. The green bars are oxygen and blue bars are water vapor. The line plot shows the detected power as a function of laser to detector distance.

To test the effect of the tissue thickness between the lungs and the laser and the detector, different slab thicknesses were tested. Results are shown in figure 26.

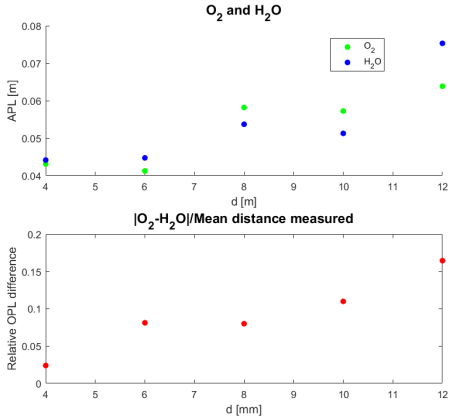

(a) Top figure shown an estimation of a know distance with the 761 nm and 820 nm laser separately. Bottom is the relative difference in distance estimated by the two lasers.

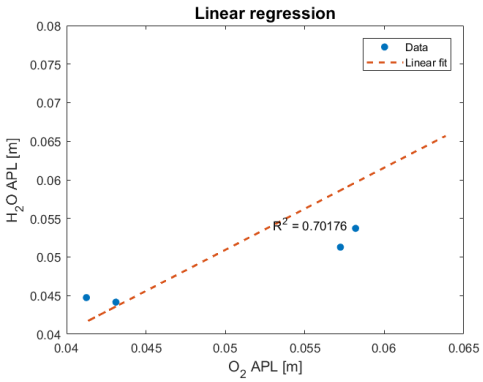

(b) Linear regression of the absorption path-length measured by the 761 nm and 820 nm laser.

Figure 26: Measurement through slabs with fixed Ldist and different thicknesses, d, to simulate tissue-lung-tissue measurements on babies of different sizes.

The estimated oxygen concentration is shown in figure 27. As can be seen, the estimate gets further and further away from the actual concentration, the thicker the slabs. Here it would be good to make new measurements to instead focus on the signal quality. The system has not been verified to work well for very low light conditions and therefore follow large uncertainties in the measurements with thick slabs.

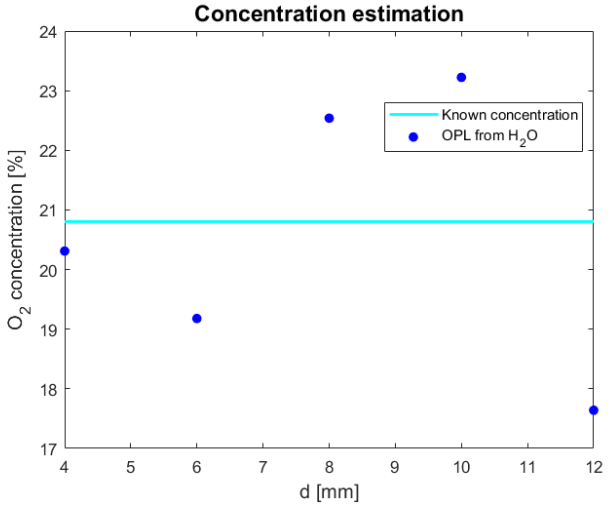

Figure 27: Oxygen concentration estimated for the humid air in the simplified lung model for different tissue thicknesses, d.

The detected power for the different thicknesses of slabs are shown in figure 28 as well as the absorption magnitude. Here it get even more clear that the detected power decreases for thick slabs. The 12 mm slab only transmits about 1 nW per laser and measurement, and this, just as in all the other phantom measurements, is with a acquisition time of 50 seconds.

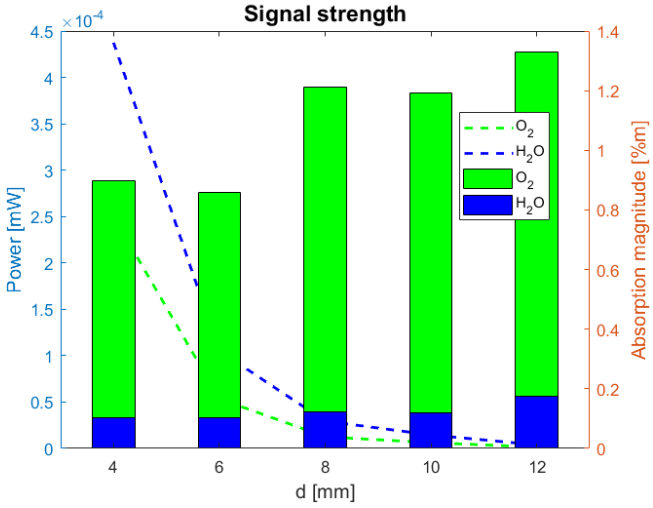

Figure 28: The bar plot shows the absorption magnitude as a function of laser to detector distance. The green bars are oxygen and blue bars are water vapor. The line plot shows the detected power as a function of laser to detector distance.

For the thicker slabs, 8, 10 and 12 mm, the absorption magnitude is higher than for the thinner slabs. A linear relation can not be found between the slab thickness and the absorption magnitude but for the tested slab thicknesses, the result indicates an increase in absorption magnitude with slab thickness, d. The thicker slabs are more likely to scatter the light further away from the center of the first slab as well as the light entering the second slab far from the center is more likely to scatter all the way to the detector.

GASMAS on infant model

In the test with the anatomical model, many different laser-detector positions were investigated but due to low power lasers and bulky laser head, only a few position combinations gave acceptable results. The positions presented in this section are marked in figure 14.

In figure 29, the APL measured and relative APL difference between the two laser wavelengths are presented. The estimates by the two laser wavelength measurements show especially good agreement for the positions 2, 3, 4, 7 and 8. The positions with laser and detector close to each other resulted in a high relative APL difference. The correlation is worse compared to the previous experiments which was done with the slab, which is expected since the received light intensities are significantly lower in these measurements.

The oxygen concentration estimation for the different detector positions is shown in figure 30. The positions 2, 3, 4, 7 and 8 does a good job estimating the oxygen concentration while the other positions underestimated it. This is in alignment with the results shown in figure 29 where measuring on the positions 2, 3, 4, 7 and 8 estimated similar APL for both wavelengths.

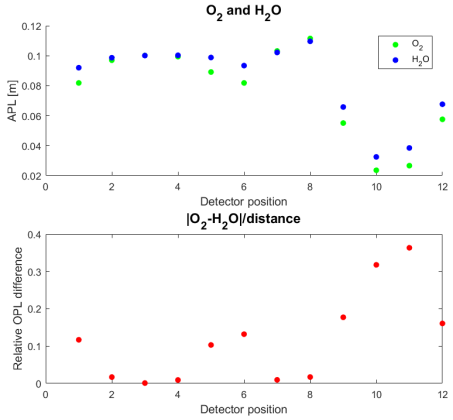

(a) Top figure shown an estimation of a known distance with the 761 nm and 820 nm laser separately. Bottom is the relative difference in distance estimated by the two lasers.

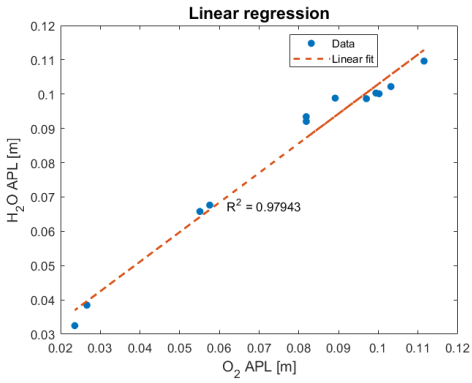

(b) Linear regression of the absorption path-length measured by the 761 nm and 820 nm laser.

Figure 29: Measurement on the anatomical torso model with a fixed laser position in the armpit and for 12 different detector positions.

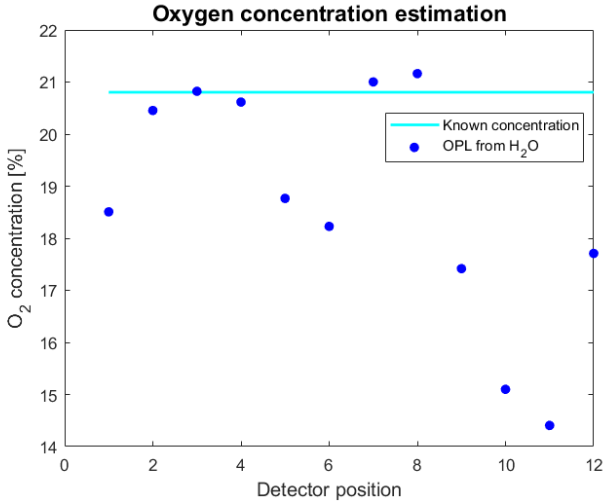

Figure 30: Absorption magnitude and detected power for the 12 measurement geometries marked in figure 14. The green and blue bars corresponds to oxygen and water vapor absorption magnitude respectively. The green and blue dashed lines mark the detected power for oxygen and water vapor respectively.

The absorption magnitude and detected power for the positions are presented in figure 31. Interesting to note is that positions 2, 3, 4, 7 and 8 have slightly higher absorption magnitude than the rest of the positions. The difference is however not big enough for a significantly better estimate. It is important to remember that the lower positions, 3, 4, 7 and 8, were more flat and it was therefore simpler to ensure that the detector stayed tight onto the phantom. Nitrogen filled transparent pockets were used for all measurements to erase any oxygen footprint, but still, low levels of oxygen could be present.

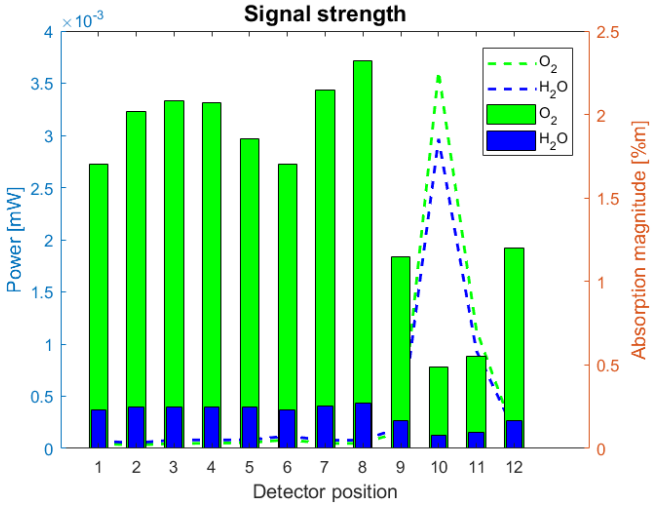

Figure 31: Absorption magnitude and detected power for the 12 measurement geometries marked in figure 14. The green and blue bars corresponds to oxygen and water vapor absorption magnitude respectively. The green and blue dashed lines marks out the detected power for oxygen and water vapor respectively.

7.3 GASMAS in-vivo measurements

It is a great opportunity to be able to perform real life measurements on a three-week old baby. It does put the system to test and makes challenges, both expected and unexpected, very evident. For the experiments on the tissue phantoms, a long acquisition time was used to account for the low power lasers in the GAS PI1 system. For measurements on infants, acquisition times must be much shorter and here acquisition times of five and ten seconds were used. Efforts were made to get reliable results to be compared to the experiments presented earlier in this thesis, but unfortunately the low light conditions did not allow it. Instead an alternative method to compare absorption signals was investigated; a method used by E. Krite Svanberg *et al.* [16] in their study of 29 newborn healthy full-term infants. It is a process to compare the plotted scan over the absorption line with a reference absorption signal performed in air and measured by the same system. With this approach the SNR could be evaluated as described in section 6.5.

First, some tests were made to ensure that the system behaved as expected. The result of those reference tests are shown in figure 32. The plots are aligned so that the left plot always shows the oxygen absorption signal whereas the right plot always shows the water vapor absorption signal. These reference measurements were conducted where the light traveled through styrofoam in air with $RH = 99.9\%$ and $T = 23°\text{C}$ to, by the long pathlength, acquire a high absorption magnitude. The middle plots are measurements through an adult forearm and, as to be expected, no absorption signal could be detected. The bottom picture shows results from an air filled adult cheek with a definite oxygen and water vapor content. This is to show that absorption signal can be acquired for in-vivo GASMAS measurements.

For the lung measurements on the baby, many tests were made, but unfortunately not many resulted in a detectable absorption signal. Out of the over 20 measure-

ments, the three with best SNR is presented in figure 33. The top plots are for an armpit to chest geometry, which is the geometry that were most tested in this experiment. Despite this, only one test had sufficiently high SNR. The middle plots are for a chest to chest geometry (both laser and detector on the same chest), which is a possible geometry for maximizing detected power with the trade-off of lower absorption magnitude by the gas. This measurement is not sufficient due to the low signal for water vapor. The bottom plots are for a stomach to stomach geometry, which of course could not be used for oxygen in lung measurements. It is still possible to find air pockets in the stomach and therefore it was tested to prove the function of the system.

This method of using the signal plots to calculate a SNR for comparable measurements has been a very successful method, which will be used in addition to the quantitative measurements in the future. It is tedious to acquire the signal plots for the GAS PI1 system and therefore not time effective. This function will be fully implemented in the pre-prototype which simplifies the measurement process.

7.4 Technical challenges

When GASMAS for lung function monitoring evolves from a laboratory setting with a still 3D-model of an infant to the neonatal clinic with preterm infants, many challenges are to be handled. Some challenges were apparent when performing the in-vivo tests and what follows is a list of a handful technical challenges to have a look out for when taking the technique for clinical studies.

- Babies move which demands a laser and a detector to keep their position throughout the measurement.
- Pressure inside the lungs are not stable, but vary around atmospheric pressure. Either acquisition times needs to be very short or an average over many breaths should be done.
- High power laser light can heat the skin. The laser power needs to be sufficient for reliable measurements but without creating harmful hot spots.
- The laser and detector should have body temperature not to irritate the baby. If attachable probes are being developed, this would be accounted for.
- The APL difference between the wavelengths can not be neglected. This can be solved, by characterizing a typical factor of APL difference or measuring with wavelengths with optical properties more close to each other, the error can be minimized.

To build a system for clinical measurements is not without challenges and it is an interesting future ahead of the GASMAS technique for lung function monitoring.

8 Conclusions and future perspectives

In this thesis work, GASMAS for measuring oxygen in the lungs of infants has been studied by simulations on a 3D-model of a preterm infant as well as in-vivo on a three week old baby. The work provides knowledge about how to simulate lung function monitoring in an laboratory setting. With the in-vivo tests, more understanding has been gained of what system requirements is to expect for future clinical studies.

The Gas PI1 system used for measurements has proven to estimate oxygen concentration with very high accuracy for high transmission and absorption pathlengths longer than 1.5 cm. For measurements on the simplified lung model and the infant model, long acquisition times were needed for the estimation to be reliable. By measurements on the simplified lung, a APL (absorption pathlength) difference between the lasers was noted, where 761 nm has an APL 20 % longer than 820 nm light for this geometry. An APL difference factor = 1.2 was therefore determined. It is certain that shorter wavelengths scattered more in tissue and how this can be accounted for when measurement geometries change must be further investigated.

The preferable measurement geometry on the 3D-model of an infant was determined to be; laser in the armpit and detector on the chest. More specifically, the positions below the nipple and quite close to the center of the chest resulted in best oxygen concentration estimation. The APL for the successful measurements was around 10 cm in the lungs which is far from the APL detected in the study of newborn babies by *E. Krite Svanberg et al.* [16] where around 2 cm APL was detected. The lung is in this thesis modelled only with humid air, which lets light scatter multiple times through the lungs without being absorbed. A real lung contains bronchial passages and alveoli that fills up much of the space inside the lungs. Future 3D-model development should account for the structure inside the lungs for a better simulation.

In this thesis, much effort has been put into calculating quantitative values of the oxygen concentration. This is very interesting when verifying the systems ability for just this task and it has been showed that the accuracy of the measurements decline when light transmission is low or absorption pathlengths are short. SNR evaluation has proven to be very useful for comparing different sets of experiments where the signal quality more easily is determined. This should more extensively be used in future measurements.

The Gas PI1 system is not the primary system for lung function monitoring. GXP Medical is developing a system dedicated for this application which will use higher power lasers for a stronger signal strength, have easy access to SNR calculation and fiber coupling to improve utility and precision of the light source. These improvements are an appreciated addition and is likely to increase the accuracy for measurements significantly, especially for low transmission measurements were signal strength is vital. The technique of using GASMAS for lung function monitoring is moving towards clinical studies, most likely in the very near future. Lung function monitoring is needed in neonatal care and GASMAS could be a technique to make non-invasive, bed-side monitoring possible.

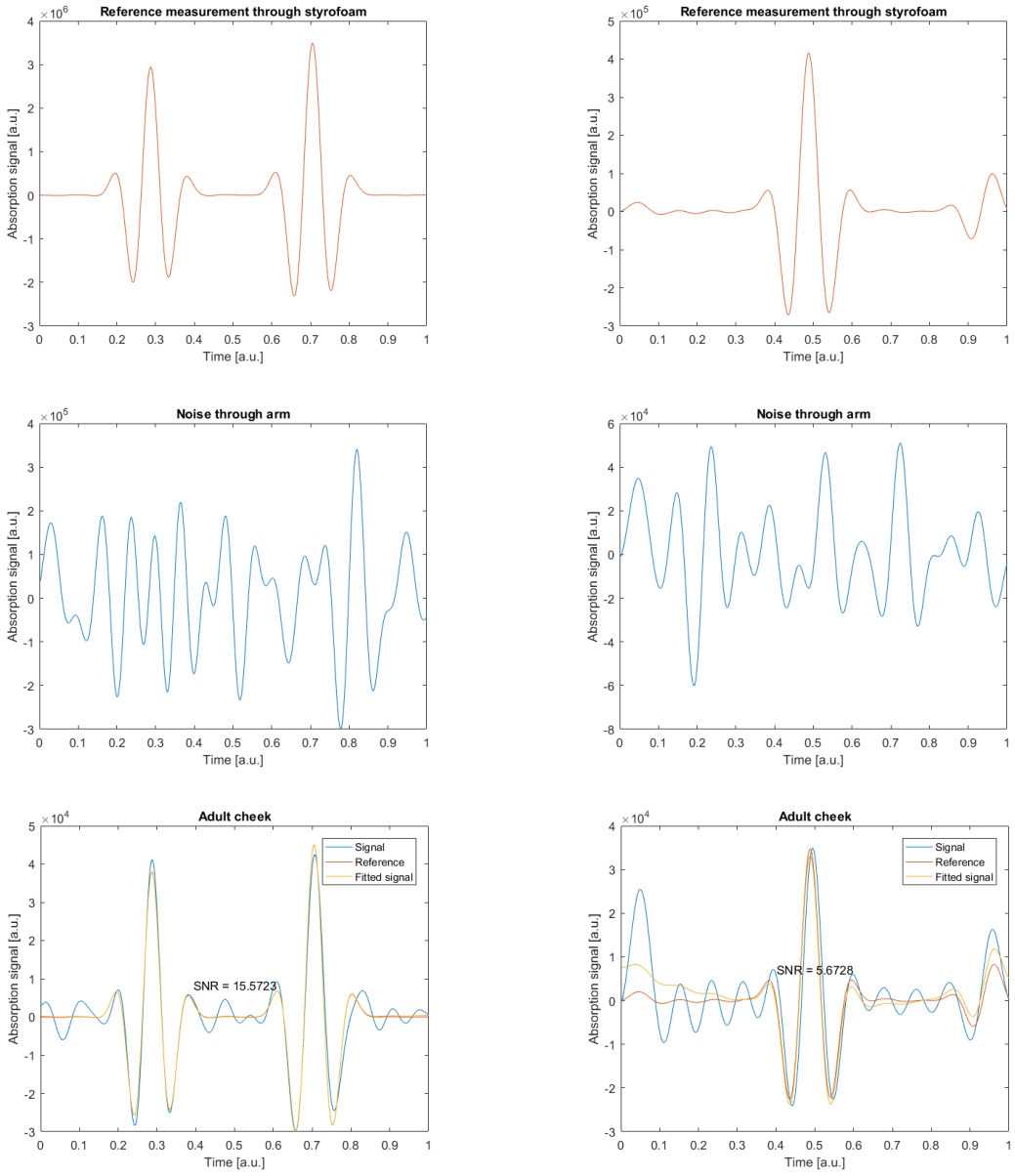

Figure 32: Reference and test measurements. O_2 absorption signal is shown to the left and H_2O absorption signal is shown to the right. The top plots are the reference measurements to be used for SNR calculations. The middle plots show measurements through an adult arm where on gaseous oxygen is present. The bottom plots show measurements through an adult cheek to test the system on a simpler in-vivo geometry.

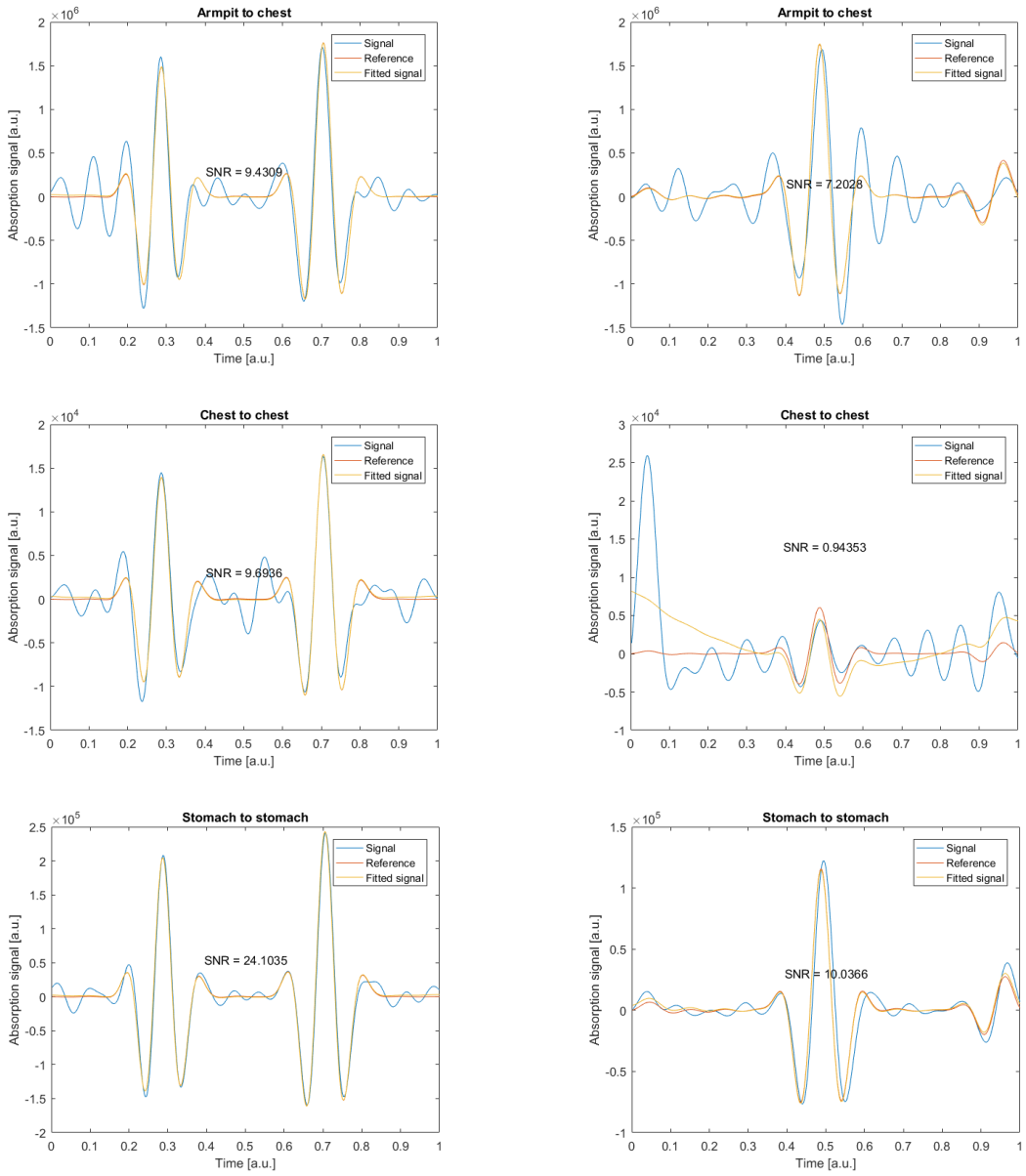

Figure 33: Measurements in-vivo on a baby. O_2 absorption signal is shown to the left and H_2O absorption signal is shown to the right.

Bibliography

[1] Gasporox. *Laboratory Headspace Gas Analyzer*. URL: http://www.gasporox.se/our-products/laboratory-instruments-2/ (visited on 09/13/2017).

[2] G. M. Hale and M. R. Querry. "Optical constants of water in the 200-nm to 200-m wavelength region". In: *Applied Optics* 12 (1973), pp. 555–563.

[3] Hamamatsu. URL: http://www.hamamatsu.com/eu/en/product/category/3100/4001/index.html (visited on 09/20/2017).

[4] J. Larsson et al. "Development of a 3-dimensional tissue lung phantom of a preterm infant for optical measurements of oxygen Laser-detector position considerations". In: *Journal of Biophotonics* TBA (2017), TBA.

[5] P. Liao. "Diode laser spectroscopy for oxygen detection in the lungs of infants". MA thesis. Lund University, Department of Physics, 2016.

[6] P. Lundin. "Laser Sensing for Quality Control and Classification - Applications for the Food Industry, Ecology and Medicine". PhD thesis. Lund University, Faculty of Engineering, 2014.

[7] P. Lundin et al. "Noninvasive monitoring of gas in the lungs and intestines of newborn infants using diode lasers: feasibility study". In: *Journal of Biomedical Optics* 18 (2013), pp. 779–796.

[8] L. Mei, G. Somesfalean, and S. Svanberg. "Pathlength Determination for Gas in Scattering Media Absorption Spectroscopy". In: *Sensors* 14 (2014).

[9] Nanoplus. URL: http://nanoplus.com/en/products/distributed-feedback-lasers/distributed-feedback-lasers-760-nm-830-nm/ (visited on 09/20/2017).

[10] P. Di Ninni, F. Martelli, and G. Zaccanti. "The use of India ink in tissue-simulating phantoms". In: *Optics Express* 18(26) (2010).

[11] S. Prahl. *Tabulated molar extinction coefficient for hemoglobin in water*. 1999. URL: http://omlc.org/spectra/hemoglobin/summary.html (visited on 04/12/2017).

[12] J.M. Richards. "A simple expression for the saturation vapour pressure of water in the range 50 to 140C". In: *Journal of Physics D: Applied Physics* 4(4) (1971), p. 876.

[13] 3D Slicer. URL: https://www.slicer.org/ (visited on 09/13/2017).

[14] L. Spinelli et al. "Determination of reference values for optical properties of liquid phantoms based on Intralipid and India ink". In: *Biomedical Optics Express* 5 (7) (2014).

[15] E. Krite Svanberg. “Non-invasive optical monitoring of free and bound oxygen in humans”. PhD thesis. Lund University, 2016.

[16] E. Krite Svanberg et al. “Diode laser spectroscopy for noninvasive monitoring of oxygen in the lungs of newborn infants”. In: *Pediatric Research* 79 (2016), pp. 621–628.

[17] S. Svanberg. “Gas in scattering media absorption spectroscopy from basic studies to biomedical applications”. In: *Laser & Photonics Reviews* 7 (2013), pp. 779–796.

[18] K. Watanabe and M. Zelikoff. “Absorption coefficients of water vapor in the vacuum ultraviolet”. In: *The Journal of the Optical Society of America* 43 (1953), pp. 753–755.